

Using airborne bathymetric lidar to detect bottom type variation in shallow waters [☆]

Chi-Kuei Wang ^{a,*}, William D. Philpot ^b

^a Department of Geomatics, National Cheng Kung University, Taiwan

^b Department of Civil and Environmental Engineering, Cornell University, United States

Received 2 November 2005; received in revised form 31 July 2006; accepted 4 August 2006

Abstract

The shape and amplitude of the bathymetric lidar waveforms (the recorded time history of the reflected lidar pulses) contain information about the attenuation of the water and the bottom reflectivity in the survey area. This study considers the factors that affect the amplitude of the bottom return and examines the use of the amplitude of the bottom return to distinguishing between different bottom types. The amplitude of the bottom return was corrected for pulse stretching and retro-reflectance due to the bottom slope based on a simple lidar radiative transfer model before the examination. Within-flightline and between-flightline variations of the bottom return were considered, both of which are related to the attenuation of water, surface wave condition, and bottom reflectivity. The major concern of within-flightline variation is the effect of surface waves on the reliability of bottom return. Between-flightline variation concerns the effect of change in viewing orientation on the bottom return from the same bottom type. A data set of Egmont Key, Florida, assuming homogeneous water clarity, was chosen to investigate the latter two effects on the bottom return signals. The result shows that the presence of surface waves is the most impeding factor that complicates the use of bottom return signal, as it can exaggerate the value (not prominent in our data) and variance of the amplitude of bottom return. A map of sand, continuous seagrass, and discontinuous seagrass ranging from the depth of 0.8 to 4.3 m was produced correctly from a single lidar flightline with limited *in-situ* information, in this case, a nadir viewing videotape concurrent with lidar survey mission. Finally, suggestions are proposed for ways to improve the production of a bottom map using the lidar waveform data.

© 2006 Elsevier Inc. All rights reserved.

Keywords: Lidar; Ocean optics

1. Introduction

Mapping of bottom types in near coastal waters has a number of important applications including modeling sediment transport, mapping and management of fish habitat, and coral reef monitoring. Sediment transport is strongly affected by bottom type and bottom roughness. For example, underwater biota can dominate hydraulic roughness and have the potential to cause spatial and temporal disturbance of the sediment (Wright et al., 1997). An improved understanding of the bottom properties would also benefit the management of coastal areas. Locating

essential fish habitat features, such as roughness, slope, vegetation, etc., would help efforts to manage and sustain the natural resources financially and ecologically (von Szalay & McConnaughey, 2002). Bottom type mapping would also be useful for monitoring the change of the size of healthy coral reef habitat area. This is particularly important given the hypothesis that the high seawater temperature, caused by global warming, leads to coral reef bleaching (Glynn, 1991). Mapping the bottom types with remote sensing would make more frequent revisits feasible and is potentially more cost effective than field data collection.

Passive, optical imaging systems have been applied to the depth and bottom type applications in various geographic and geologic areas (Bagheri et al., 1998; Mobley et al., 2005). These systems have the advantage of being able to cover large areas in a short time, but are difficult to calibrate, very limited in the range of detectable depths, and are typically limited by the

[☆] When this work was conducted, Chi-Kuei Wang was with Cornell University. During the writing of this manuscript, Chi-Kuei Wang was with the University of Southern Mississippi and then with National Cheng Kung University.

* Corresponding author.

E-mail address: chikuei@mail.ncku.edu.tw (C.-K. Wang).

depth of penetration and the accuracy of the bathymetry derived from the spectral imagery. The accuracy of depth determination with passive optical systems is limited in part by the inherent sensitivity of the systems and in part by the sensitivity of the observations to changes in water optical properties (Kohler, 2001). Nonetheless, passive, hyperspectral imaging systems have potential for delineating bottom types when the spectral reflectance of different bottom types is sufficiently distinct (Hochberg & Atkinson, 2000; Tsai & Philpot, 2002).

Another possibility is to use the amplitude of the bottom return from an Airborne Lidar Bathymetry (ALB) system as an indicator of the bottom type. ALB is designed to measure the depth of the water based on the two-way travel time of a short pulse of light between the water surface and the bottom. An advantage of the lidar system is that it is capable of measuring the water depth from 1.5 m down to 60 m, depending on the water clarity (Abbot et al., 1996; Guenther et al., 2000; Steinvall et al., 1994). The depth limit is often described as being two to three times the Secchi depth. This is far superior to the depth penetration of passive optical systems which are generally limited to no better than 1.5 Secchi depths.

Bathymetric lidar systems use lasers that emit a short green pulse in order to maximize penetration in water for a wide range of water types. At longer wavelengths water absorption increases very significantly. At shorter wavelengths, scattering and absorption by substances in the water increase rapidly, decreasing the penetration depth. Obviously, since lidar is a monochromatic system, it can only provide a monochromatic map of bottom reflectance. This is the primary drawback for the lidar systems because only one variable can be used to characterize the bottom, and is in stark contrast to passive imaging systems, especially hyperspectral sensors, that can use spectral information to assess the bottom type in optically shallow waters. This suggests that a combination of lidar and passive imaging systems may well be optimal for bottom classification (Bissett et al., 2005; Wright & Brock, 2002). However, here we are concerned with the use of lidar data alone.

In order to detect both the surface and the bottom, and to determine the distance between them, the entire time history of the lidar return signal through the water path (the waveform) must be recorded. This waveform contains information about both the change in water transmission with depth and bottom reflectance. Not all lidar systems save the full waveform for subsequent analysis and verification. This study takes advantage of a wealth of data stored from survey missions by the Scanzing Hydrographic Operational Airborne Lidar Survey (SHOALS) that stores the entire resulting waveform for each laser pulse and uses these data to characterize the bottom material and to detect the associated variations in the survey area.

A generic bathymetric lidar waveform is shown in Fig. 1. The waveform can be viewed as three parts: the water surface return, the water volume backscattering, and the bottom return. The surface return is the first and usually the strongest component of the return. It can be quite variable, however, as it depends on the roughness of the water surface and can disappear entirely due to specular reflection when the water surface is flat calm. Volume

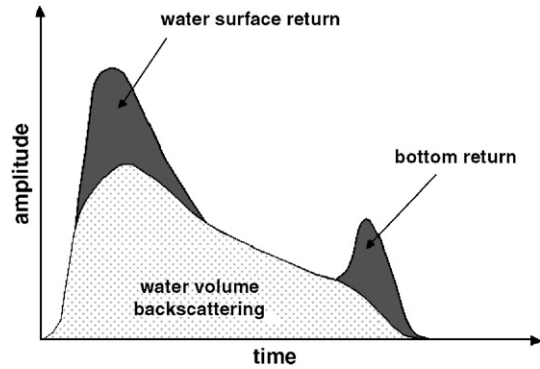


Fig. 1. Generic bathymetric lidar waveform.

backscattering by the water begins as the pulse enters the water, and increases until the pulse is entirely within the water. The water volume backscattering attenuates exponentially with respect to the product of depth and the water diffuse attenuation coefficient once the whole pulse is submerged in the water. As seen in Fig. 1, the bottom return is the last signal that arrives at the sensor. Losses at the air–water interface and the specific attenuation rate of the water will affect the amplitude and shape of the bottom return.

The amplitude of the bottom return from a bathymetric lidar contains information about the reflectance of the bottom cover at the lidar wavelength. However, there are a number of other factors that can also have a significant effect on the amplitude of the bottom return. Some of these factors are quite predictable and relatively easily accounted for. These would include the effects of the depth, water attenuation, and the pulse stretching that result when the bottom slopes relative to the incident angle of the lidar. Others, typically environmental in nature, may be identified easily enough, but are much more difficult to account for. Wave double focusing effect (see Section 3.1), for example, can both amplify and introduce substantial variability in the amplitude of the bottom return.

In this research, the potential of using a lidar system to discriminate different bottom types is evaluated by examining the data set collected at Egmont Key, Florida. Although the data are obtained from one particular lidar system, the basic principle can be applied to other systems. The data set from Egmont Key provides a simple scenario that consists of two bottom materials, seagrass and sand, in relatively turbid waters. With the assumption of homogenous water clarity throughout the survey area, the simple conditions at Egmont Key provide insight into the environmental effects on the bottom return signal.

2. Materials and methods

2.1. The SHOALS system

The version of the SHOALS system used in this study employed a scanning, pulsed Nd:YAG laser transmitter capable of emission at both the fundamental wavelength of 1064 nm (infrared) and the frequency-doubled wavelength of 532 nm (green) with a ~ 6 ns pulse width and a pulse repetition rate of 400 Hz. The output power of the laser is 15 mJ (1064 nm) and

5 mJ (532 nm). The received signals are digitized into 1 ns bins and the entire resulting waveform for each pulse is stored. The SHOALS scan pattern describes an arc ahead of aircraft with the center of the beam held at a constant nadir angle (the angle between the vector of receiver or transmitter and normal vector of the surface, c.f. θ in Fig. 2) of 20° (Irish & Lillycrop, 1999). The diameter of the laser footprint on the water surface is maintained at approximately 2.4 m regardless of the altitude of the aircraft (Sosebee, 2001).

The SHOALS system is typically operated at an altitude of 200 m and a speed of 60 m/s, which corresponds to a survey swath and horizontal spot density of 110 m and 4 m (Irish & Lillycrop, 1999). The position of each lidar sounding is determined using a combination of the inertial navigation system and the global positioning system.

2.2. Basic models and concepts

Although SHOALS does not explicitly use the amplitude information of the bottom return to retrieve the depth (Guenther et al., 1996), the amplitude information is still stored in the data as part of the waveform. The amplitude of the bottom return is obtained by subtracting the extended exponential curve of the volume backscattering return to the time bin of the peak value of the bottom return from the lidar waveform (Guenther, 2001). This amplitude, however, is a function of a number of factors (depth, water clarity, bottom slope, etc.), not just the bottom reflectance. In order to better understand and characterize these effects, it is useful to model the process using a simple lidar radiative transfer model.

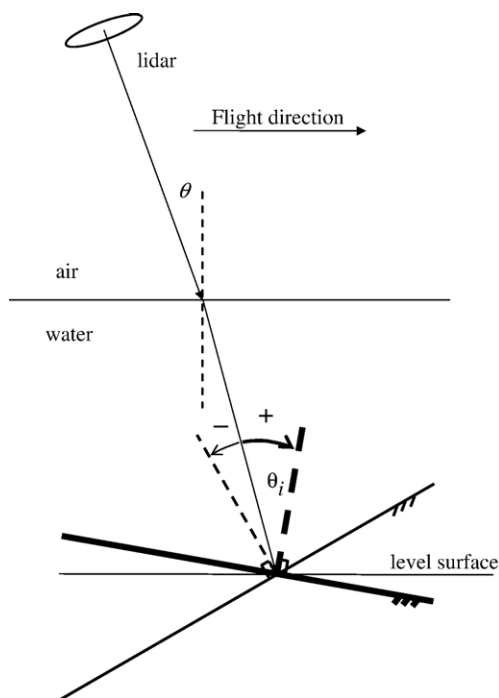


Fig. 2. Schematic diagram showing the refraction of an incident light beam passing from air through water and reflecting from the sea bottom. The nadir angle is defined by θ .

The laser pulse transmitted from the lidar system through the water and reflected back from the ocean bottom to the receiver is attenuated exponentially with depth. Since the nadir angle and the altitude are well maintained during the survey mission, and all the system loss terms are well controlled, we use a simple mathematical description of the process (Guenther, 1985):

$$P_R = P_T W \rho \exp(-2k_{\text{sys}}D) \quad (1)$$

where P_R is the received power [watts], P_T is the transmitted power [watts], W combines all the system factors and is taken as a constant [steradians], ρ is the irradiance reflectance of the bottom [steradian⁻¹], k_{sys} is the attenuation coefficient specific for the lidar system and the water type [m^{-1}], and D is bottom depth [m], positive downward from the water surface. The system term, W , actually includes the expression $(D+H)$ where H is the altitude of the aircraft, but since the lidar is always at the altitude $H > 200$ m and the bottom depths considered in this paper are always relatively shallow, $D < 13$ m, the effect of depth on W is negligible. Taking the natural log of Eq. (1) yields:

$$\ln(P_R) = \ln(P_T W) + \ln(\rho) - 2k_{\text{sys}}D \quad (2)$$

From this equation, it is clear that if the losses of the lidar system in W are all well controlled and the transmitted power is constant, the natural log of the return signal, $\ln(P_R)$, is a linear function of the natural log of the reflectance of the bottom, $\ln(\rho)$, and the system attenuation length, $k_{\text{sys}}D$. In an area for which the system attenuation coefficient, k_{sys} , is constant, bottom types with distinct reflectance will then describe parallel lines in a plot of $\ln(P_R)$ versus D . Hence, the accuracy of detecting bottom material change will be dependent on the accuracy of the depth estimate and the uncertainty in the system attenuation coefficient.

2.3. Data correction procedures

In this study we assume that the water is optically homogeneous over each study area and therefore will not address corrections for the system attenuation here. There are, however, several other factors which will affect the amplitude of the bottom return that cannot be generally assumed to be negligible, even locally. The most important of these is a correction for the relative slope of the bottom as it relates to the Bi-directional Reflectance Distribution Function (BRDF) (Haner et al., 1998). There is an additional effect associated with the relative slope – pulse stretching – that will lower the apparent reflectance.

2.3.1. Correction for bottom reflectance using laboratory measurements

The bottom slope affects the bottom return since reflectance is a function of illumination and viewing angle, in addition to material type. The general relationship is described by the BRDF (Haner et al., 1998). In the absence of measured BRDF values for the bottom types considered here, it is common to assume that the surfaces are Lambertian. This assumption may generally be realistic for flat sand bottoms (Mobley, 1994) but is

likely to be less than ideal for other cases and may be questionable even for sandy bottoms for reflectance of lidar signals.

For a given bottom reflectance, the bottom return from a perfectly diffuse (Lambertian) surface, will be a maximum for a surface that is perpendicular to the direction of incidence and, for purely geometric reasons, can be expected to decrease as the cosine of the relative slope. The Lambertian surface is defined as (Mobley, 1994):

$$r(\theta_i, \phi_i \rightarrow \theta_r, \phi_r) = \frac{\rho}{\pi} \cos\theta_i, \quad (3)$$

where r is the radiance reflectance, θ and ϕ are the nadir angle and azimuth angle (the angle between the projection of the receiver and transmitter on the surface and any defined forward vector, positive counterclockwise) in spherical coordinates, and i and r denote the incident and reflected light, respectively. θ_i is shown in Fig. 2. Thus the apparent reflectance will be dependent on the relative slope of the bottom and the laser illuminating direction.

ALBs are almost always built in a monostatic configuration, which means the transmitter and the receiver are aligned and share an overlapping field of view (FOV). Frequently the transmission and detection optics are located coaxially. In this case, the bottom return signal results from retro-reflectance, i.e., light reflected back to the sensor in exactly the reverse direction of the incident light. There is substantial documentation (Hapke, 1993; Meister et al., 2001) of the reflectance being significantly higher in this direction due to an absence of shadowing. This phenomenon is called the “hot spot” in remote sensing image processing (Hapke, 1993; Meister et al., 2001). However, due to the lack of data of the BRDF of real world materials (Voss et al., 2000), especially with the retro-reflectance measurement, the “hot spot” effect is modeled using data from a laboratory measurement and used as a first order correction for the effect due to slope orientations.

In order to make an initial estimate of the correction, we begin with the assumption that all the bottom materials are equally diffusive materials at the wavelength of 532 nm with a BRDF similar to that of a 50% reflectance standard, Spectralon (Labsphere, Inc.). The light source was a tungsten halogen light source (LS-1) from Ocean Optics, Inc. The LS-1 emits a continuous spectrum from ultra-violet to infrared, but only the data of the wavelength of 532 nm was analyzed. The retro-reflectance probe (Ocean Optics Inc.) was used to simulate the transmitter and receiver configuration of a lidar system. It is a tight bundle of seven optical fibers in a stainless steel ferrule with six fibers surrounding one fiber in the middle. The illumination is provided by the six outer fibers and the reflected radiation is viewed through the central fiber. The result of the retro-reflectance of the 50% diffuse reflecting Spectralon and the theoretical radiance reflectance of Lambertian surface based on Eq. (3) are shown in Fig. 3. The values are normalized to the value at 0° (nadir looking). The result of the measurement shows a linear relationship of reflectance with the nadir angle:

$$f(\theta_i) = -0.0123\theta_i + 1.086, \quad 0^\circ \leq |\theta_i| < 90^\circ, \quad (4)$$

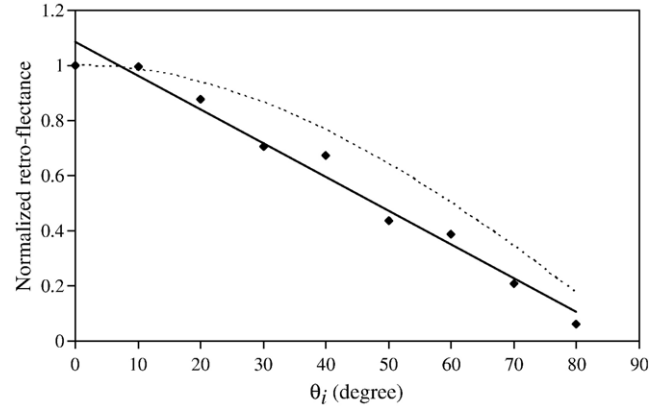


Fig. 3. Comparison of the retro-reflectance measurement of the 50% diffusively reflecting Spectralon and the theoretical values of Lambertian surface. The points are the measured data. The solid line is the linear regression of the data points. The dash line is the theoretical value of a Lambertian surface (Eq. (3)). The values are normalized to the value at 0°, respectively, where the normal of the material surface is parallel to the illuminating light. θ_i is defined in Fig. 2.

where θ_i is the same as that used in Eq. (3). Specifically, θ_i is the lidar incident angle in the plane of incidence defined by the laser beam and the bottom normal vector (Fig. 2). With oblique laser incidence, the positive direction is set when the bottom normal vector tilts away from the lidar.

2.3.2. Correction for pulse stretching

Another effect of the bottom slope that requires a correction procedure is pulse stretching. The energy in the bottom return is a function of time. When the pulse is reflected from a surface that is perpendicular to the viewing angle, the pulse will be in its most compressed form. As the reflecting surface is tilted away from the viewing angle, the pulse will be reflected first from the portion of the surface closest to the source and then from portions of the surface farther from the source. The reflected energy is then distributed over a longer time than the incident energy and the maximum return per unit time is reduced. Since the maximum return is used as the measure of the bottom reflectance, the pulse stretching effect will reduce the apparent reflectance. An analytical simulation has demonstrated the bottom slope effect on bottom pulse stretching (Steinval & Koppari, 1996; Steinval et al., 1994). Rather than try to base the correction on strictly geometric arguments, we use the analytical predictions of Steinval and Koppari (1996). The results of the modeling, shown in Fig. 4, illustrate the relationship between the lidar incident angle on the bottom (i.e., nadir angle θ_i) and the correction coefficients. Since only the range from -40° to 40° is reported, an extrapolation is used to obtain correction coefficients outside of this range. The relationship is:

$$g(\theta_i) = \begin{cases} 0.9651 \exp(0.0457\theta_i), & -90^\circ < \theta_i \leq 0^\circ \\ 1.0021 \exp(-0.0359\theta_i), & 0^\circ \leq \theta_i < 90^\circ \end{cases} \quad (5)$$

The lidar incident angle on the bottom is required for both the slope correction and the pulse stretch correction. Since we have the bathymetry both for the point in question and several adjacent points, the local bottom slope is calculated by

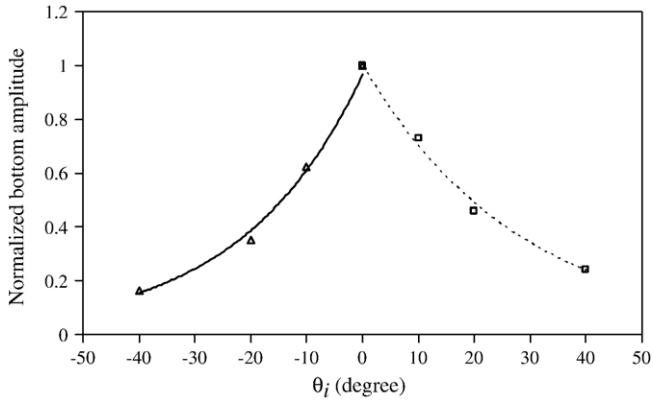


Fig. 4. The relationship between lidar incident angle and bottom pulse peak amplitude. The triangle and square markers show the situations when the bottom is toward and away from lidar, respectively. The solid and dash lines are the exponential regressions of associated data points. θ_i is defined in Fig. 2.

determining the normal of the facet consisting of the sounding for the target point and the nearest two soundings in the forward direction. The lidar incident angle is computed as the arc cosine of the dot product of the normal and the source vector.

The slope correction procedure consists of three steps:

- 1) Compute an estimate of the slope based on ALB depth measurements of adjacent points and the lidar incident angle on the bottom.
- 2) Correct for the retro-reflectance based on the simple laboratory observations at nadir-viewing, i.e., $\theta_i=0$.
- 3) Correct for the pulse stretching based on the analytical simulation of Steinvall and Koppari (1996) for nadir-viewing, i.e., $\theta_i=0$.

Essentially, Eq. (1) is now modified by the inclusion of two terms, $f(\theta_i)$ (Eq. (4)) and $g(\theta_i)$ (Eq. (5)):

$$P_R = P_T W \rho f(\theta_i) g(\theta_i) \exp(-2k_{\text{sys}} D). \quad (6)$$

Rearranging Eq. (6), taking the natural log of both sides, and introducing a new notation, P'_R we have

$$\ln(P'_R) = \ln\left(\frac{P_R}{f(\theta_i)g(\theta_i)}\right) = \ln(P_T W) + \ln(\rho) - 2k_{\text{sys}} D. \quad (7)$$

Eq. (7), similar to Eq. (2), modifies the bottom return signal in order to correct for the slope effects on the signal. These corrections were applied to all data discussed below.

2.4. Data descriptions

This study is based on data taken from bathymetric mapping missions flown at Egmont Key, Florida, which is an island located outside of Tampa Bay between two navigational channels. The west shoreline of Egmont Key has changed significantly over the past 100 years, but the shoreline on the east side, near the study site, has changed little over that same period of time (Kling, 1997). Also, as a barrier island, the east shore is more protected from currents and storms in Gulf of Mexico. This

is significant because the data used for ground truth were not collected simultaneously with the lidar bathymetry data and we assume that the data are comparable in terms of the location of changes in bottom type. The SHOALS data were acquired at an altitude of 400 m with a swath width of 220 m and transverse and longitudinal sample spacing of 6 m and 8 m, respectively, on May 15th, 2000. The surveyed area is between $27^\circ 33.71'N$ and $27^\circ 38.05'N$ in latitude and between $-82^\circ 50.56'E$ and $-82^\circ 44.76'E$ in longitude.

SHOALS was equipped with a nadir-looking color video camera to visually record the water condition during each survey flight (Irish & Lillycrop, 1999). The videotape provides useful information of the surveyed area that was often needed to evaluate the effect of environmental factors that might affect the lidar signal return, such as white caps. However, the videotape quality was often poor and, in extreme cases, sun glint from the water surface saturated the camera. Also, the resolution of the video image was not comparable to that of the lidar data.

Data from other institutions and agencies were used as ground truth to supplement the videotape image. A National Aerial Photography Program (NAPP) georeferenced image was used as the primary reference map for Egmont Key area. It was collected at an altitude of 6000 m above mean terrain on January 7, 1999. The spatial resolution of the NAPP photograph is 0.5 m. A seagrass map acquired from the Florida Geographic Data Library (FGDL) was also used to provide ground truth (Fig. 5). The data represented on the map were collected by Florida Marine Research Institute (FMRI) (FGDL, 2000). The limited description of continuous and discontinuous seagrass in the FMRI data was supplemented by personal communication with researchers familiar with the area (Crewz, 2001; McRae, 2001; White, 2001). According to their field observations, there are three primarily seagrass species on the east coast of Egmont Key. These are *Halodule wrightii*, *Thalassia testudinum*, and *Syringodium filiforme*. The rest of the area on the east coast is sandy bottom with shelly inclusions (Crewz, 2001).

The NAPP photo has served as the primary ground truth map for Egmont Key because it has spatial detail that is superior to the mission videotape and the FMRI seagrass map. Although there was an approximate 17 month gap between the NAPP photo mission and the lidar mission, with no intervening storms (NOAA, 2000) the main bottom features defined by the seagrass delineation had not changed substantially, judging from a qualitative comparison with the mission videotape.

3. Results and discussion

In the ideal case (i.e., constant laser pulse power, no gravity waves on the scale of the lidar footprint, a flat ocean bottom and uniform water clarity), changes in the amplitude of the bottom return would be due largely to differences in bottom type. This section will focus on environmental effects on the bottom return signal and the feasibility of distinguishing different bottom types when the environmental effects cannot be ignored.

The effect of the environment can vary within a flightline and also between flightlines. Within-flightline variations include wave effects in dispersing the lidar pulse as well as real

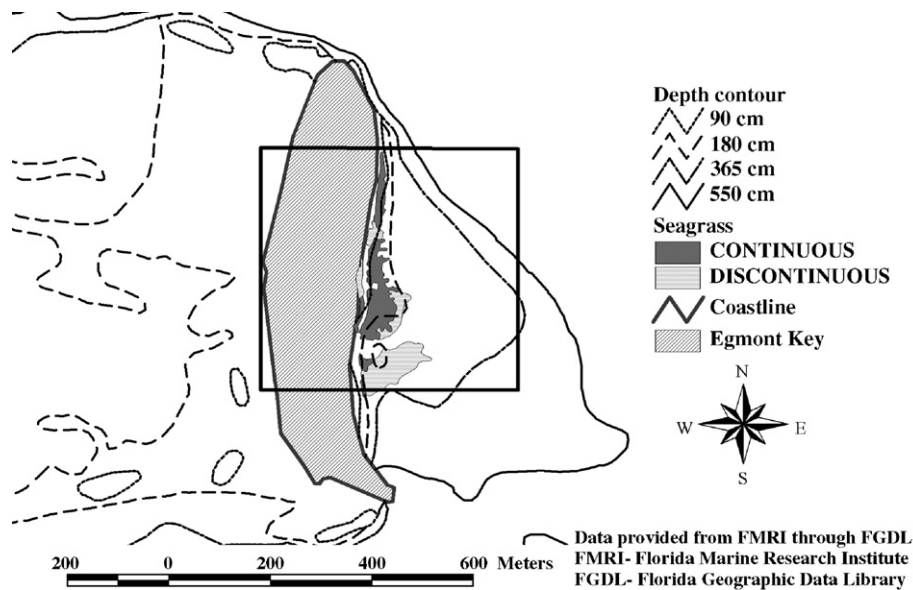


Fig. 5. Spatial distribution of seagrass at the east coast of Egmont Key, Florida. The square box corresponds to the area of Fig. 6.

bottom variability. Between-flightline variations are largely a matter of differences in the viewing direction of the SHOALS sensor. These include wave effects, and bottom slope issues.

3.1. Within-flightline variations

3.1.1. Wave effects

Two flightline segments from Egmont Key, study sites 1 and 2 in Fig. 6, were selected for the analysis of the wave effects. They were chosen so as to cover the largest possible depth range within each flightline. These data are also selected only from the edge of the flightlines heading south in order to minimize any effects of changes in the viewing direction, a topic which will be dealt with separately in Section 3.2. The bottom type within both study sites is predominantly sand. (The FMRI data indicates all sand, but small scattered dark patches in the mission tape indicate the possibility of another bottom type.) The bottom slope range in these areas is less than 5° . This provides a nearly ideal situation with minimum bottom variation to examine the wave effect on SHOALS data.

Scatter plots of the natural log of the corrected amplitude of the bottom return versus depth using Eq. (7) for the study sites 1 and 2 are shown in Fig. 7. The expectation is that the data for a single bottom type should describe a straight line in the scatter plot as stated in Section 2.2. For both study sites the bottom type is uniformly sand, and both scatter plots show the same trend, but with a significant amount of variability about the line of best-fit obtained from linear regression analysis ($R^2=0.593$ for study site 1; $R^2=0.622$ for study site 2). Since it is the deviation in y -intercept from this line that will be the main indicator of a change in bottom type, it is important to consider the nature of this variability when the bottom type is constant.

In order to examine the depth dependence of the variability, the mean and standard deviation of the bottom return signals from study sites 1 and 2 were calculated by binning the data in 0.5 m intervals except where there was insufficient data for a

meaningful result. The results are plotted in Fig. 7 and summarized in Table 1.

As can be seen in both scatter plots, data points at shallower depths are more dispersed than those at greater depths. It is likely that this is due to double focusing, an effect due to the presence of water surface waves and the fact that the transmitter and the receiver are in a monostatic configuration. Double focusing (also known as the aureole; Minnaert, 1993) is related to the brightness pattern seen on the bottom of a pool when the water surface is anything other than flat calm. The term double focusing describes the fact that both the laser light and the FOV of the receiver are focused by the water surface.

Double focusing has been described using a ray tracing model (McLean & Freeman, 1996) and in analytical analysis (Abrosimov & Luchinin, 1999; Luchinin, 1987). This phenomenon causes both the mean values and the variance of the lidar bottom return signals in shallow regions to increase unevenly with respect to the depth. The depth of shallow maximum is the depth at which the maximum magnification of the received signals occurs. Around that depth, the variance of the bottom return signals also reaches its maximum value (Abrosimov & Luchinin, 1999; Luchinin, 1987; McLean & Freeman, 1996). The effect is a function of water wave geometry, which can be related to wind speed. However, without direct observations of the water surface or wind speed, the effect is not predictable. The effect is only important in relatively shallow waters, i.e., at depths of approximately 7 m or less. The depth of the maximum fluctuation of the bottom return signal indicates the approximate depth at which the laser beam is focused by the water surface (McLean & Freeman, 1996). It should affect the trend in the scatter plot by increasing the fluctuation near the focus depth and increasing the amplitude of the bottom return near the same depth by $\sim 20\%$ (McLean & Freeman, 1996). However, the scatter plot data do not exhibit the expected increase in the mean amplitude corresponding with the increase in variance. The data at the depth of 3 m to 4 m, where the largest fluctuations exist

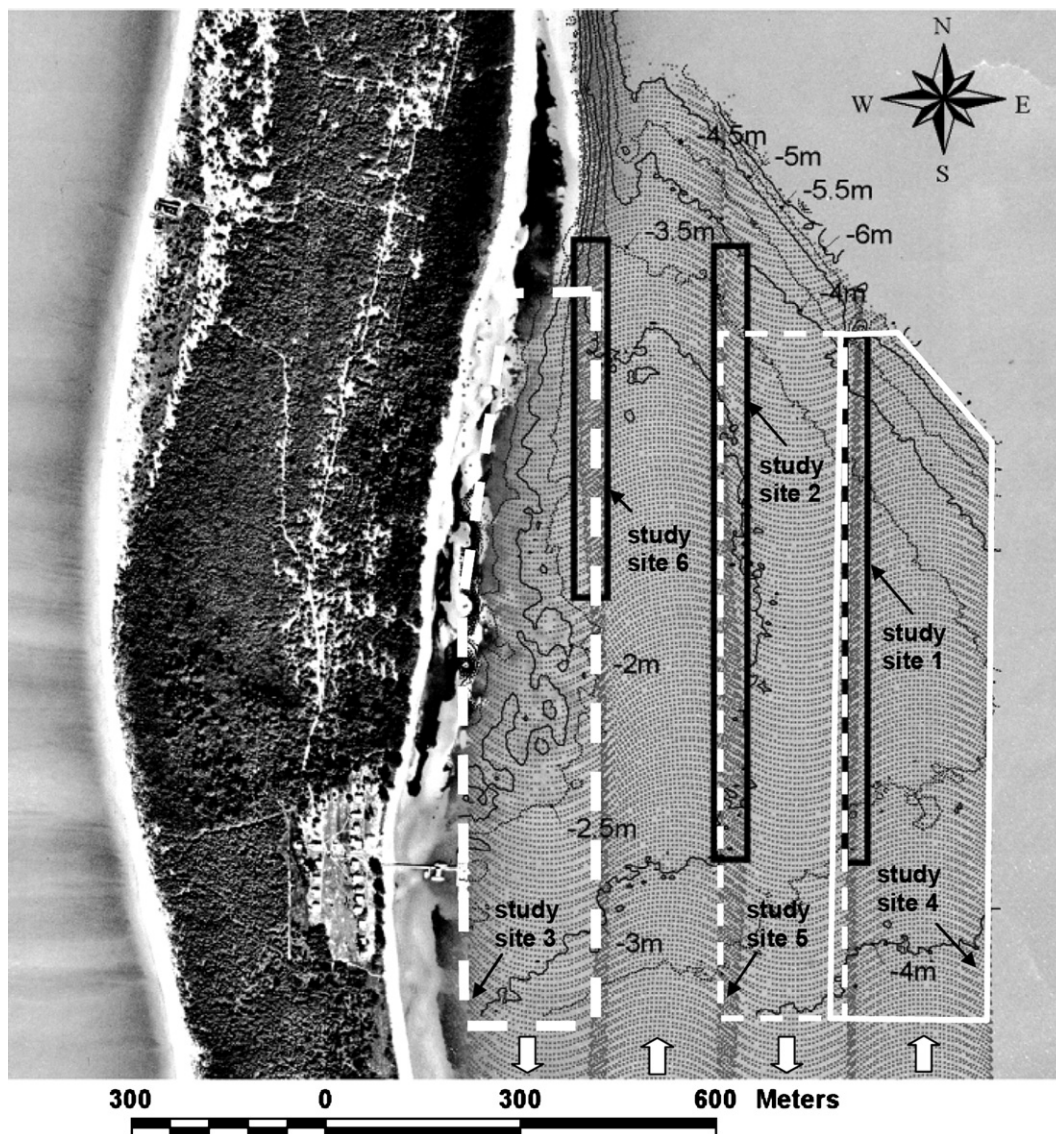


Fig. 6. A map showing study sites at Egmont Key. The dot points are the lidar sounding data. The arrows near the bottom of the image indicate the flightline directions. The depth contours are generated from SHOALS depth output. The data from the edge of the South-headed flightlines at study sites 1 and 2 and that at study sites 3 to 6 are used for the examination of within-flight variations. The overlap data at study sites 1, 2, and 6 are used for the examination of between-flightline variations.

should be greater than those shown in Fig. 7. One explanation for this discrepancy is that turbid water at Egmont Key tends to increase scattering thereby masking the double focusing effect.

3.1.2. Bottom effects

At least part of the variability in bottom reflectance is due to the inherent reflectance of different materials. This is precisely the information that we would hope to use to delineate areas of different bottom types. To consider this case, study site 3, located along the eastern shore of Egmont Key, was selected because it contains two distinctive bottom types, sand and seagrass. Study site 3 is located near shore with water depth from 0.8 m to 4.3 m. At this site the slope is gentle as can be seen by the contours in the map of this area (Fig. 6).

Seagrass is substantially darker than sand at 532 nm, due largely to absorption by photosynthetic pigments. Seagrass reflectance is also more variable than sand for several reasons:

(1) the density of seagrass may vary significantly; (2) apparent reflectance will depend on the substrate (sand, silt, etc.); (3) seagrass reflectance may be altered by a covering of scum or epiphyte (Smith, 2001).

As discussed in Section 2.2, if the difference in the amplitude of the bottom return were only due to differences in the inherent reflectance and the depth of the water, then each discrete bottom type would align along parallel paths in a scatter plot. A scatter plot of the data from study site 3 and the corresponding color-coded map of the area are shown in Fig. 8. Assuming that the change in bottom type is the dominant effect in Fig. 8a, the cluster of samples known to be pure sand was used to compute a best-fit straight line. Using the slope of this line as a guide, the scatter plot was then divided into three parallel ranges that would correspond to different bottom types. The three regions were then color-coded and illustrated on the map of that data (Fig. 8b). This procedure requires a knowledge of the *in-situ*

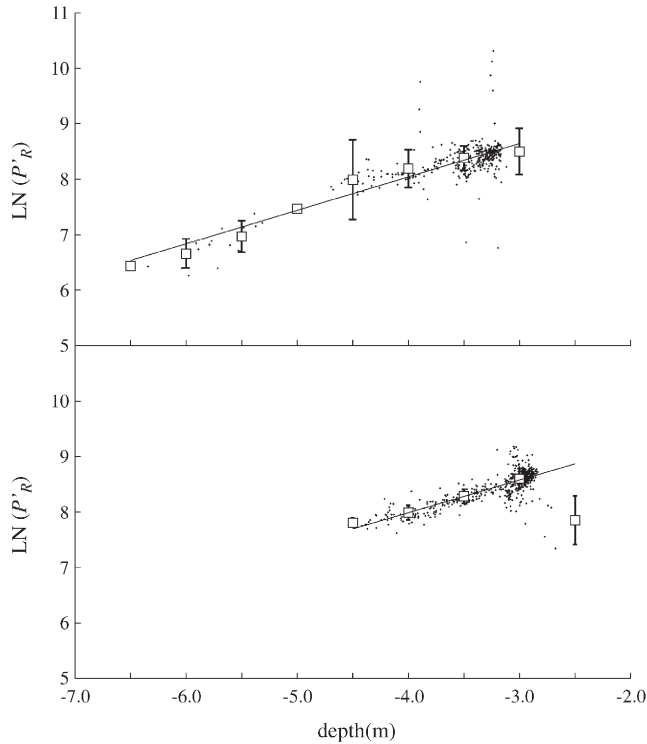


Fig. 7. Scatter plots of natural log of corrected bottom return versus water depth: (a) study site 1, (b) study site 2. Only the data from the flightline flown toward south is used. The dots are the lidar data. The squares are the means of lidar data at 0.5 m interval. The error bars show one standard deviation range at 0.5 m interval.

information provided in this case by the mission videotape. The bounding box in Fig. 8a shows that the samples of pure sand that are determined from the mission videotape were highly reflective regardless of depth. The bounds of the three regions were selected by trial and error in order to match the delineation of seagrass shown in the mission videotape (not shown here). Comparing the seagrass map acquired by FMRI (Fig. 5), the mission videotape (not shown here), and the color-coded map of study site 3 (Fig. 8b), it appears that both the continuous and discontinuous seagrass beds are delineated by the one channel (532 nm) lidar data. This is true even in the deeper waters where the mission video is too poor to show any contrast.

The detailed structure within the discontinuous seagrass – not delineated in the FMRI map – is also depicted in the color-coded map of study site 3. In the scatter plot and the color-coded map of study site 3, blue refers to dark seagrass and red to bright seagrass. The dark seagrass area matches well with continuous seagrass and the bright seagrass matches well with discontinuous seagrass in Fig. 5.

The scatter plot behavior seen in Fig. 8, is most easily explained using the concept of a mixed sample. The ground area illuminated by a single lidar pulse represents a single sample. Seagrass is often locally inhomogeneous and, even at its most dense, the substrate can often be seen when looking down through the seagrass. Thus, the illuminated spot always contains two materials, sand and seagrass. When the depth increases, less sunlight gets to the bottom, resulting in a lower density of

seagrass. The apparent reflectance of seagrass pixel will increase if sand is present in the pixel, and the proportion of the two within a sample then determines the apparent reflectance of the seagrass. This simplified model requires that the seagrass reflectance be the same for different life stages and at different depths. The report of an experiment conducted in a nearby location off Mullet Key, Florida (Fort Desoto Park) with seagrass species *H. wrightii*, the major seagrass species in Egmont Key, draws two conclusions that are relevant to this research. First, the chlorophyll *a* content per green area of seagrass does not vary with light condition, which implies that the reflectance of seagrass will not change with depth. Second, the green biomass is positively correlated to the downwelling irradiance, which implies that more light can support more green biomasses (Neely, 1999). Since the location of the cited study is within 15 km of Egmont Key, genetic/biological differences due to the geographical separation are minimized. Thus, we justify the assumption that chlorophyll *a* content of *H. wrightii* in Egmont Key does not change during depth or life stage. However, this remains a possible source of undocumented error.

The dark seagrass area (blue) shown in Fig. 8 is a dense seagrass bed that dwells on, and almost completely covers the background sand. It also suggests that the seagrass is not covered by sand. The bright seagrass (red) indicates the presence of a relatively sparse seagrass bed. This may be new seagrass beds emerging from sand or a more established bed that is partially covered by suspended sand trapped by seagrass. Another possibility is that the habitat seagrass dies off. Any of these introduce the existence of sand in the illuminated pixel and increase the apparent reflectivity of seagrass. Without direct field confirmation, the true situation cannot be identified. Since the presence of seagrass within a pixel can be from zero to total occupancy, the observed variation in apparent reflectance of the seagrass is broad.

Using a subset of soundings that correspond to sand from study site 3, the mean and standard deviations of the corrected bottom return signal at each depth were calculated. The scatter plot of sand in study site 3 is shown in Fig. 9. The dashed lines represent one standard deviation from the center line in the linear regression of the data and the square markers represent the mean value of the standard deviation from the depth of 4 m to 1.5 m at 0.5 m interval, up and down along the ordinate. The data gap between the depth of ~3 m to ~3.5 m exists because,

Depth (m)	2.5	3	3.5	4	4.5	5	5.5	6	6.5
<i>Study site 1</i>									
Mean		8.50	8.38	8.19	7.98	n/a	6.96	6.66	n/a
Standard deviation		0.42	0.22	0.34	0.18	n/a	0.28	0.26	n/a
Averaged standard deviation: 0.28									
<i>Study site 2</i>									
Mean	7.85	8.59	8.28	7.98	7.81				
Standard deviation	0.43	0.18	0.12	0.13	0.08				
Averaged standard deviation: 0.19									

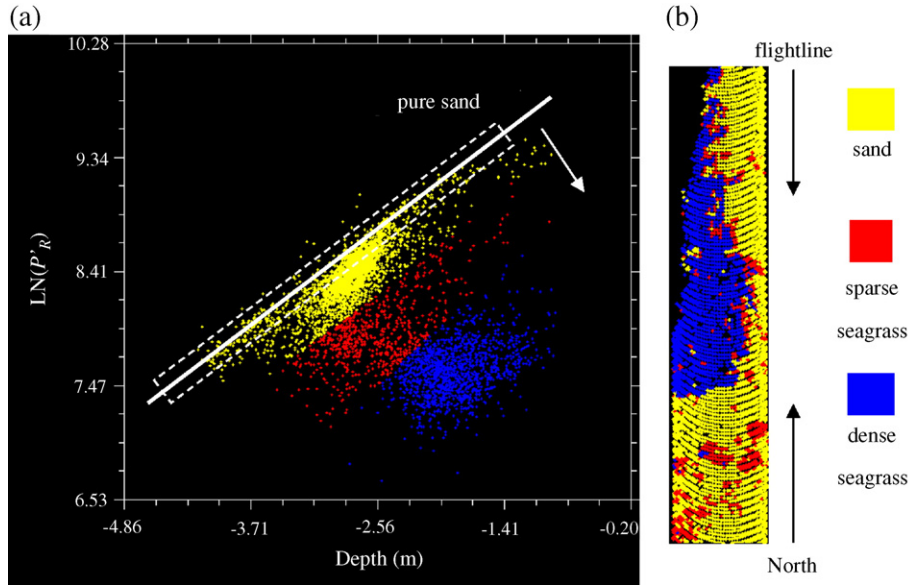


Fig. 8. (a) Scatter plot of natural log of corrected bottom return versus water depth and (b) corresponding color-coded map of study site 3. The dashed box indicates the samples of pure sand determined from the mission videotape.

at these depths, the bottom is occupied by seagrass. The one standard deviation band contains 77% of the data as opposed to the value of 67% for a normal distribution function. This suggests that, if the linear regression curve and averaged standard deviation of one bottom material can be determined based on information from other sources, one could reasonably divide the scatter plot into regions representing different bottom types based on the slope of the curve and a scale based on the variance of the known bottom type.

Other, more subtle environmental factors may affect the amplitude of the bottom return. Two subsets, sites 4 and 5, of Egmont Key data (see Fig. 6) were selected for illustration. A scatter plot and color-coded map of study site 4 are shown in Fig. 10. The corresponding data for site 5 are shown in Fig. 11. Sand is the only bottom material in both study sites. It is

assumed that the water surface and water clarity characteristics are homogenous within each study site.

Depths at site 4 range from 2.75 m to 6 m, and form two distinct clusters at greater depths. Red is assigned to the data points with larger amplitude and green is assigned to those with lower amplitude for depths greater than 3.8 m. As seen in Fig. 10b, the red area is on the northern slope and the green area is on the southern slope. A similar distribution appears in shallower waters, with depths ranging from 3.25 m to 3.8 m. The blue region, which has larger signal amplitude, is toward the north and the magenta region, which has lower signal amplitude, is toward the south. This means that sand on the north slope consistently appears brighter than that on the southern slope.

A very similar pattern is observed in the data from study site 5. As at site 4, red is assigned to points with larger amplitudes; green is assigned to those with lower amplitudes for depth greater than 3.34 m. Blue is assigned to data points with larger amplitudes; magenta is assigned to data points with lower amplitudes from depth of 2.97 m to 3.34 m. The red and blue points occupy the north region of the map, and the green and magenta points occupy the south region (Fig. 11b). Again, the sand appears brighter at the north of Egmont Key than at the south end.

For either flightline, one could argue that the differences in apparent reflectance could be a result in differences in bottom slope, surface waves, or other factors. However, since data from the two study sites are collected from two flightlines flown in opposite directions, the directional effects, such as bottom slope, surface wave, etc. are factored out as contributors to the patterns in the scatterplot.

The contours shown in Fig. 6 indicate that the bottom slope at the north is steeper than that at the south. This implies a more dynamic water environment at the north and a relative calm water environment at the south. Due to the relatively calm environment at the south the reflectance of sand may be reduced

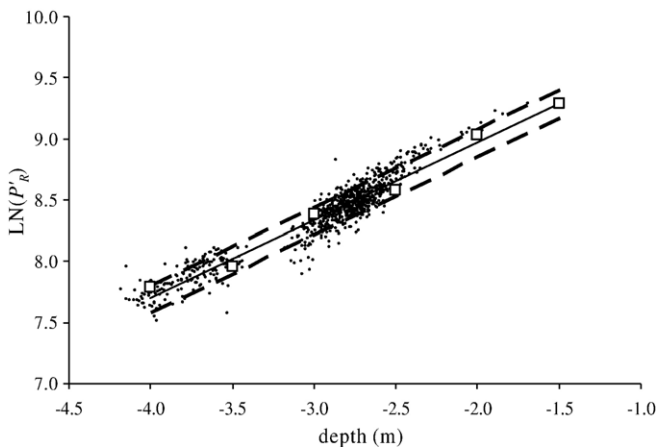


Fig. 9. Scatter plot of natural log of corrected bottom return versus water depth of data from a sand area in study site 3. Also shown is the best-fit regression line (solid line) of the lidar data, the one standard deviation band (dash line), and the mean value at 0.5 m interval (square mark).

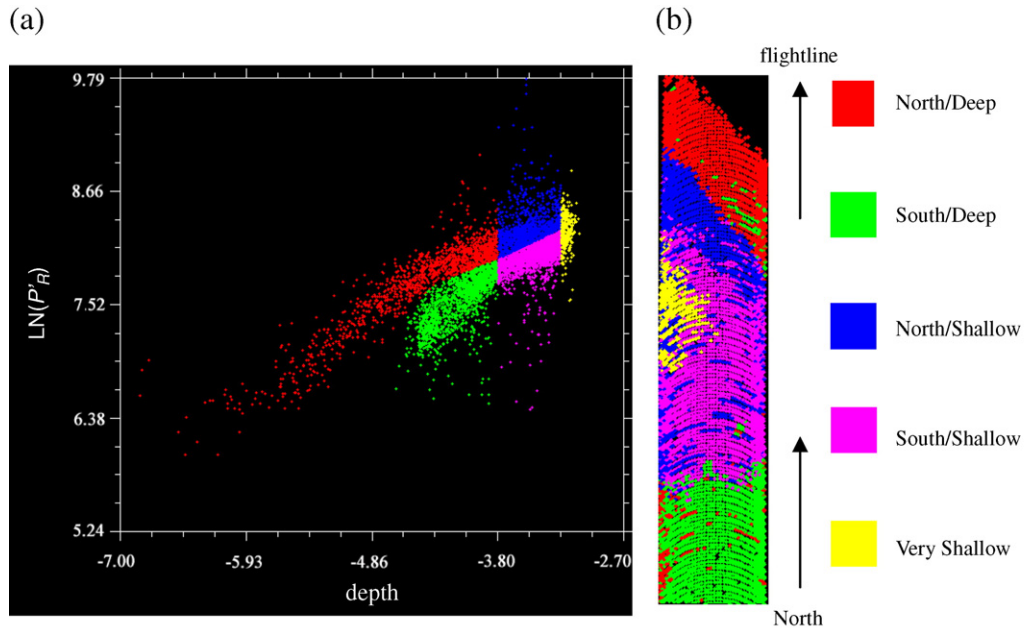


Fig. 10. (a) Scatter plot of natural log of corrected bottom return versus water depth and (b) corresponding color-coded map of study site 4.

by scum, debris, or small patches of seagrass. In contrast, the brighter reflectance of the sand on the north slope is consistent with sand that is continually disturbed, mixed and washed by the currents. A second possibility is that the surface of the northern site is rougher, possibly due to the presence of sand waves. There is some evidence that, for retro-reflectance, reflectance may increase with the roughness of the surface as more surface facets become oriented toward the lidar (Clavano & Philpot, 2004; Oren & Nayar, 1996; Wolff et al., 1998). Either or both of these factors would also help to explain the fact that the deviation at sites 1 and 2 (Fig. 7) are greater than that of sand in site 3 (Fig. 9).

3.2. Between-flightline variations

Like other airborne sensors, SHOALS collects data by flying back and forth over the survey area. The flightlines are parallel to each other and are offset by a few hundreds of meters. The exact amount of the offset depends on the design of the mission. Two adjacent flightlines overlap each other by at least a few meters to ensure that there are no gaps in the survey area. This flying pattern, coupled with the change in viewing orientation of the lidar, means that there is a significant range of viewing directions over a flightline and, where the flightlines overlap, the same point on the water surface is viewed from different directions.

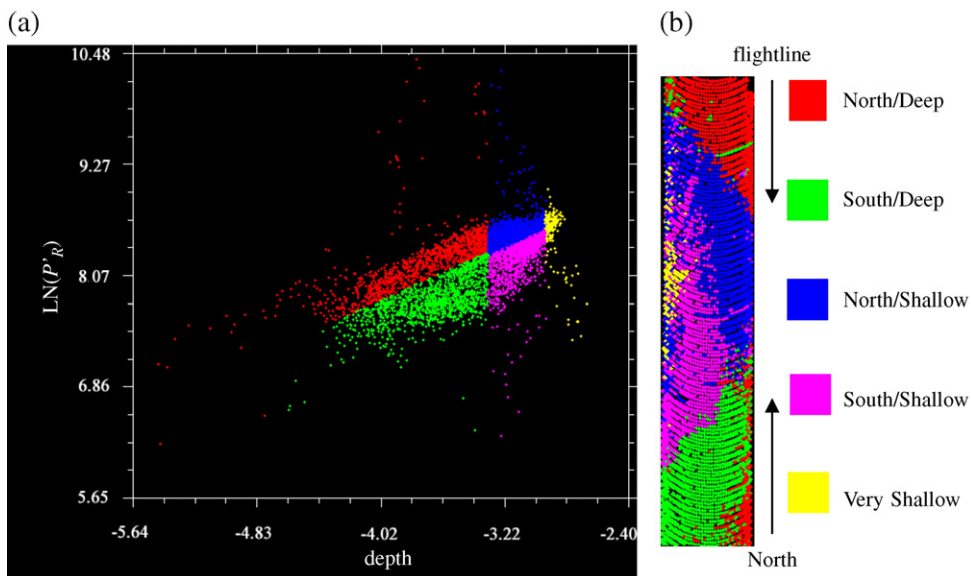


Fig. 11. (a) Scatter plot of natural log of corrected bottom return versus water depth and (b) corresponding color-coded map of site 5.

Three study sites are selected to examine the effect of opposite viewing directions: study sites 1, 2 and 6 in Egmont Key. They are illustrated in Fig. 6 with study site 1 in water with depths of 3 m to 7 m. Study site 6 is the closest to shore with the depth of 2.5 m to 3.5 m. Study site 2 is at intermediate depths of 2.6 m to 4.5 m. For each study site data are included from the overlapping edges of two flightlines oriented in opposite directions, one flown toward the south and one flown toward the north. The scatter plots and the best-fit lines of these data can be seen in Fig. 12a, b and c. All three areas are selected to have only sand within their coverage.

As shown in Fig. 12a (study site 6), the bottom return signal inferred from the best-fit line of the southward flightline is greater than that of the northward flightline at all depths. Due to limited range of water depth and possible double focusing effect of surface wave, the slopes of these two best-fit lines are questionable. They are only the indication of the difference between data collected from opposite flightlines for study site 6. In Fig. 12b, scatter plot of study site 2, the bottom return signal collected from the flightline flown toward south is noticeably greater than that from the flightline toward the north. The trends of the two data sets start to merge at depths greater than 4 m or so. In Fig. 12c, the scatter plot of study site 1 shows clearly that two data trends are merging from the depths of 3 m to 7 m. The

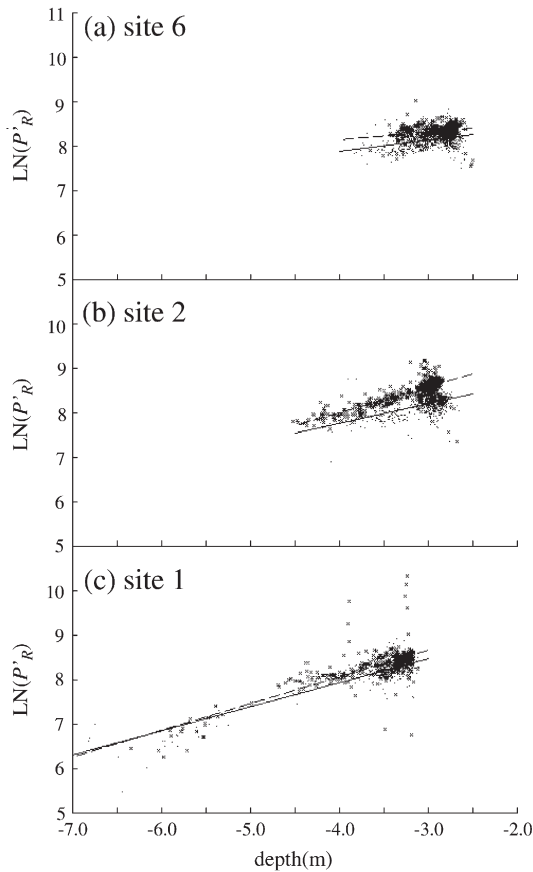


Fig. 12. Scatter plots of natural log of corrected bottom return versus water depth: (a) site 6. (b) site 2, (c) site 1. Data from opposite flightlines are used. The solid and dotted lines represent the best-fit line for the data from the flightlines flown toward north (dots) and south (crosses), respectively.

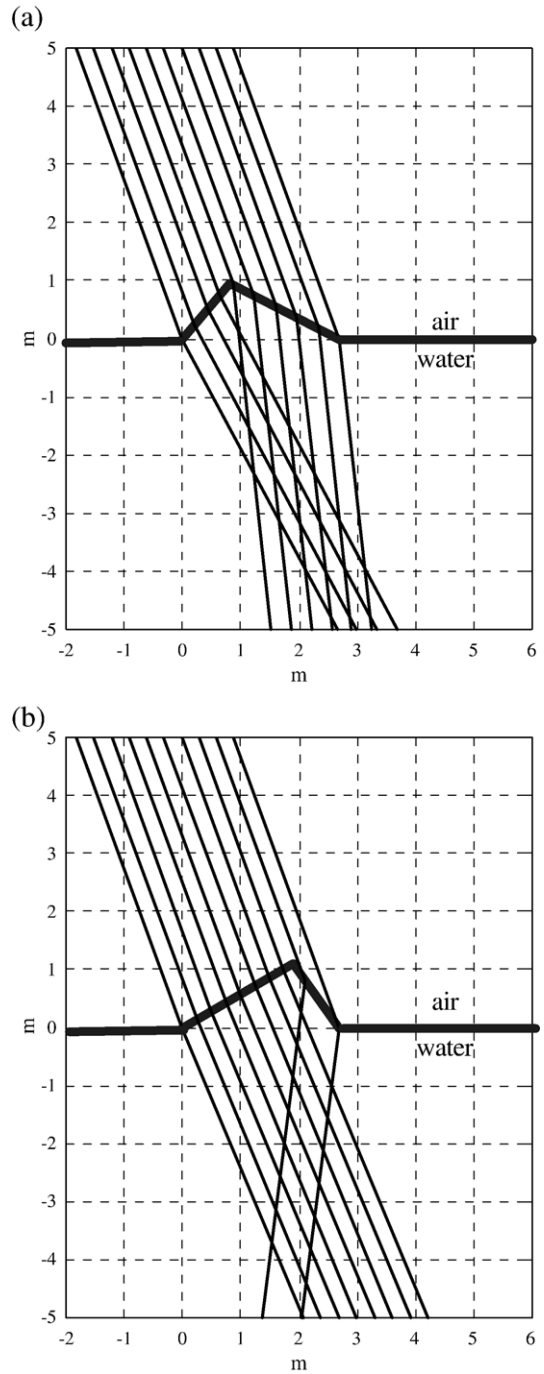


Fig. 13. Comparisons of the refracted light rays of the same incident illumination distribution entering an asymmetric wave traveling in opposite directions.

increased value and variation of bottom return signal at the depth of 3.25 m and 4 m can be explained by the wave double focusing effect as discussed in Section 3.1.

With the absence of wind direction and strength measurements, we suspect that the trend discrepancy of bottom return signals from adjacent flightlines with opposite directions at shallow depth (<4 m for Egmont Key data set), which is inferred from the best-fit lines, is due to an asymmetry induced by the geometry of the water surface waves relative to the incident direction of the lidar. Surface waves can alter the

apparent return depending on their symmetry and orientation. Both the wind strength and direction, and the geometry of the ocean floor, can cause surface wave asymmetry. The incident light field can then be distorted by an asymmetric wave as shown in Fig. 13, which illustrates the refraction of 10 light rays representing the light field of the laser. The wave shown in Fig. 13 is a simplified schematic realization of an asymmetric wave. The two waves have the same geometry except they are horizontally reversed or equivalently, the same wave, surveyed from opposite directions. As a result of wave double focusing, the bottom return signal will be affected differently in each case. As was seen with wave double focusing, when the water depth increases, the effect of an asymmetric surface wave is lessened.

4. Summary and conclusions

Two corrections were applied to lidar data in order to correct for effects introduced by bottom slope relative to the looking angle of the lidar system. Both the amplitude and shape of the recorded waveform are dependent on the slope of the bottom relative to the lidar viewing angle. The results of an analytical simulation of waveform distortion caused by bottom slope (Steinval & Koppari, 1996) were adopted to normalize the signal to the value at nadir. The signal was then corrected for the non-Lambertian directional reflectance (retro-reflectance) based on results of a laboratory experiment conducted to normalize the measured reflectance.

Beyond the slope corrections, there are several other factors that complicate the discrimination of bottom types based on the corrected amplitude of the bottom return. Since some of these factors are sensitive to the direction of observation, we considered two situations separately, within-flightline variations and between-flightline variations.

By exploring data within a specific flightline, the confusion introduced by the orientation and asymmetry of water surface waves can be excluded. In this case the signal is sensitive to a variety of environmental conditions and geographic/geologic characteristics that can result in misclassification of bottom materials. The most typical problem is a “mixed pixel” problem. The footprint of a single sounding may contain more than one bottom type, e.g. seagrass and sand. The observed amplitude can vary continuously from the reflectance of pure sand to a dense seagrass canopy. It is also probably impossible to distinguish between a sparse, continuous seagrass bed and a group of small dense patches of seagrass on a sand substrate when both occupy the same percentage of area within the lidar footprint. This serves to emphasize that, at most, the bottom return signal is a single-channel estimate of reflectance and that any two bottom types with similar reflectance characteristics in that one channel will be indistinguishable.

The presence of surface waves complicates the analysis via wave double focusing effect. In theory, both the amplitude and variance of the bottom return signal will be exaggerated due to focusing by the waves (Abrosimov & Luchinin, 1999; Luchinin, 1987; McLean & Freeman, 1996). (Only the increase in variance was apparent in our data.) The effect reaches its maximum at the depth where downwelling light is most strongly focused and is

dependent on the dominant slope spectrum of the surface waves. The variance becomes less when water depth increases and becomes constant at depths where the light is well scattered.

The asymmetry of the surface waves also plays an important role affecting the return signal. It distorts the signal by altering the downwelling light field complicating the comparison of bottom return signals from two different flightlines. Like the wave double focusing effects, the asymmetry effects are less pronounced in strongly scattering environments making the effect less important in turbid waters or at greater depths (Fig. 12).

Although average wave height information can be extracted from lidar data, the wavelength and curvature are not available at the scale that is significant for the wave focusing effect.

Regardless of these complicating factors, we showed that with limited knowledge of the *in-situ* data, in our case, a nadir viewing videotape recorded simultaneously with the lidar survey mission, the lidar data can correctly produce a map of sand, continuous/dense seagrass, and discontinuous/sparse seagrass (Fig. 8). Knowledge of the spatial distribution of these bottom types can further facilitate fishery habitat management (von Szalay & McConnaughey, 2002) or monitoring the spatial distribution of sediment (Wright et al., 1997).

Currently the intent is to make maximum use of existing lidar bathymetry data to discriminate among bottom types based only on the amplitude of the bottom return. The following recommendations address the issue of creating a bottom map of a survey area, across several flightlines.

- 1) Compute the bottom slope for each lidar sounding.
- 2) Correct the bottom return signal for pulse-stretching effects due to the bottom slope.
- 3) Correct the bottom return signal for the retro-reflectance due to the bottom slope.
- 4) Use the dominant material within each flightline as a baseline. The assumption here is that, if the water clarity is invariant over the flightline, the samples for the dominant material will form a linear feature in the natural log of bottom signal versus depth scatter plot. This will provide a baseline and an estimate of the local variance that can be used to estimate when a significant change in reflectance has occurred.
- 5) Use the mean and variance of the dominant material to characterize changes in reflectance. For each flightline, identify a linear feature in the scatter plot, which represents the combined attenuation of water and lidar optics for a constant bottom type. Obtain the slope of the linear feature by simple linear regression and use the slope to normalize every bottom return signal to the same depth, for example depth just below the water. Iterate the same process in other flightlines and make the values at the overlap area match. If the double focusing effect is not negligible, the classification may be in error at shallower depths.

Acknowledgement

This work was supported by the Hydrographic Science Research Center of the Southern Mississippi Grant number

USM-GR006627-07 and by the US Army Corps of Engineers Contract number DACW42-00-C-0032.

References

- Abbot, R. H., Lane, D. W., Sinclair, M. J., & Spruing, T. A. (1996). Lasers chart the waters of Australia's Great Barrier Reef. *Proc. SPIE, Vol. 2964* (pp. 72–90).
- Abrsimov, D. I., & Luchinin, A. G. (1999). Signal statistics of lidar sounding of the upper ocean through its rough surface. *Izvestiya, Atmospheric and Oceanic Physics, 35*, 266–272.
- Bagheri, S., Stein, M., & Dios, R. (1998). Utility of hyperspectral data for bathymetric mapping in a turbid estuary. *International Journal of Remote Sensing, 19*, 1179–1188.
- Bissett, W. P., DeBra, S., Kadiwala, M., Kohler, D. D. R., Mobley, C., Steward, R. G., et al. (2005). Development, validation, and fusion of high resolution active and passive optical imagery. *Proc. SPIE, Vol. 5809* (pp. 341–349).
- Clavano, W., & Philpot, W. D. (2004, October 25–29). Reflections and the focusing effect from an ideal three-dimensional rough surface. *Proc. Ocean Optics, Vol. XVII. Australia: Fremantle*.
- Crewz, D., (2001). Personal communication, July, 2001.
- Florida Geographic Data Library (FGDL). (2000). *FLORIDA GEOGRAPHIC DATA LIBRARY DOCUMENTATION* on CD. <http://www.fgdl.org>
- Glynn, P. W. (1991). Coral-reef bleaching in the 1980s and possible connections with global warming. *Trends in Ecology and Evolution, 6*, 175–179.
- Guenther, G. C. (1985). *Airborne laser hydrography: System design and performance factors*. U.S. Department of Commerce, NOAA professional paper series 385 pp.
- Guenther, G. C. (2001). Personal communication, October, 2001.
- Guenther, G. C., Cunningham, A. G., LaRocque, P. E., & Reid, D. J. (2000, June 16–17). Meeting the accuracy challenge in Airborne Lidar Bathymetry. *Proc. EARSeL-SIG-Workshop LIDAR, Dresden/FRG*.
- Guenther, G. C., Thomas, R. W. L., & LaRocque, P. E. (1996). Design considerations for achieving high accuracy with the SHOALS bathymetric lidar system. *Proc. SPIE, Vol. 2964* (pp. 2–25).
- Haner, D. A., McGuckin, B. T., Menzies, R. T., Bruegge, C. J., & Duval, V. (1998). Directional-hemispherical reflectance for Spectralon by integration of its bidirectional reflectance. *Applied Optics, 37*, 3996–3999.
- Hapke, B. (1993). *Theory of reflectance and emittance spectroscopy* (pp. 455). New York: Cambridge University Press.
- Hochberg, E. J., & Atkinson, M. J. (2000). Spectral discrimination of coral reef benthic communities. *Coral Reefs, 19*, 164–171.
- Irish, J. L., & Lillycrop, W. J. (1999). Scanning laser mapping of the coastal zone: The SHOALS system. *ISPRS Journal of Photogrammetry and Remote Sensing, 54*, 123–129.
- Kling, J. A., (1997). *Geologic History and Morphodynamics of Egmont Key, Hillsborough County, Florida*, M.S. Thesis, University of South Florida, Tampa, Florida, 145 pp.
- Kohler, D. D. (2001). *An Evaluation of A Derivative Based Hyperspectral Bathymetric Algorithm*. Ph.D. Thesis, Cornell University, Ithaca, New York, 113 pp.
- Luchinin, A. G. (1987). Some properties of a backscattered signal in laser sounding of the upper ocean through a rough surface. *Izvestiya, Atmospheric and Oceanic Physics, 23*, 725–729.
- McLean, J. W., & Freeman, J. D. (1996). Effects of ocean waves on airborne lidar imaging. *Applied Optics, 35*, 3261–3269.
- McRae, G. (2001). Personal communication, July, 2001.
- Meister, G., Rothkirch, A., Spitzer, H., & Bienlein, J. K. (2001). Large-scale bidirectional reflectance model for urban areas. *IEEE Transactions on Geoscience and Remote Sensing, 39*, 1927–1942.
- Minnaert, M. (1993). *Light and color in the outdoors*. New York: Springer-Verlag 417 pp.
- Mobley, C. D. (1994). *Light and water: Radiative transfer in natural waters*. New York: Academic Press 592 pp.
- Mobley, C., Sundman, L., Davis, C., Bowles, J., Downes, T., Leathers, R., et al. (2005). Interpretation of hyperspectral remote-sensing imagery by spectrum matching and look-up tables. *Applied Optics, 44*, 3576–3592.
- Neely, M. B. (1999). Somatic, respiratory, and photosynthetic responses of the seagrass *Halodule wrightii* to light reduction in Tampa Bay, Florida including a whole plant carbon budget. In S. A. Bortone (Ed.), *Seagrasses: Monitoring, ecology, physiology, and management* (pp. 33–48). New York: CRC press.
- NOAA, (2000). *The 2000 Atlantic Hurricane Season*. <http://www.nhc.noaa.gov/2000.html>. Accessed on 5 May 2000.
- Oren, M., & Nayar, S. K. (1996). Generalization of Lambert's reflectance model. *ACM Computer Graphics Proceedings, SIGGRAPH, Vol. 94*.
- Smith, F. G. F. (2001). *Methods of Remote Sensing for The Mapping of Seagrass*. Ph.D. Thesis, University of South Carolina, Columbia, South Carolina, 134 pp.
- Sosebee, C. R. (2001). *Improvement of the Land/Water Discrimination Algorithm for the US Army Corps of Engineers Scanning Hydrographic Operational Airborne Lidar System*. M.S. Thesis, Cornell University, Ithaca, New York, 99 pp.
- Steinval, O. K., & Koppari, K. R. (1996). Depth sounding lidar: An overview of Swedish activities and future prospects. *Proc. SPIE, Vol. 2964*. (pp. 2–25).
- Steinval, O. K., Koppari, K. R., & Karlsson, U. C. (1994). Airborne laser depth sounding: System aspects and performance. *Proc. SPIE Vol. 2258, Ocean Optics, Vol. XII* (pp. 392–412).
- Tsai, F., & Philpot, W. D. (2002). A derivative-aided hyperspectral image analysis system for land-cover classification. *IEEE Transactions on Geoscience and Remote Sensing, 40*, 416–425.
- von Szalay, P. G., & McConnaughey, R. A. (2002). The effect of slope and vessel speed on the performance of a single beam acoustic seabed classification system. *Fisheries Research, 54*, 181–194.
- Voss, K. J., Zhang, H., & Al, C. (2000, October 15–20). Bi-directional reflectance distribution functions (BRDF) of benthic surfaces in the littoral zone. *Proc. Ocean Optics, Vol. XV. Monaco*.
- White, W. (2001). Personal communication, July, 2001.
- Wolff, L. B., Naryar, S. K., & Oren, M. (1998). Improved diffuse reflection models for computer vision. *International Journal of Computer Vision, 30*, 55–71.
- Wright, C. W., & Brock, J. C. (2002, May 20–22). EARRL: A lidar for mapping shallow coral reefs and other coastal environments. *Proc. 7th International Conference on Remote Sensing for Marine and Coastal Environments, Miami, Florida*.
- Wright, L. D., Schaffner, L. C., & Maa, J. P. Y. (1997). Biological mediation of bottom boundary layer processes and sediment suspension in the lower Chesapeake Bay. *Marine Geology, 141*, 27–50.